Check for updates

ADVANCED OPTICAL MATERIALS
www.advopticalmat.de

Half-Integer Topological Charge Polarization of Quasi-Dirac Bound States in the Continuum

*Edoardo De Tommasi, Silvia Romano, Vito Mocella, Fabrizio Sgrignuoli, Vittorino Lanzio, Stefano Cabrini, and Gianluigi Zito**

The non-trivial polarization topology of bound states in the continuum (BICs) provides new strategies in nanophotonics. The polarization topology depends on the geometric parameters and energy-momentum dispersion of the system and can be engineered to add specific functionalities for light molding. Herein, such a possibility is investigated by studying the topology of the polarization states associated with the optical field radiated by BICs when Dirac-cone-degeneracy is lifted. The opening of a pseudogap in the Dirac cone dispersion of square-lattice dielectric photonic crystal slabs is achieved by tuning the slab thickness. First, the emergence of half-integer topological charges without the requirement of BIC annihilation is theoretically shown, which instead occurs when in-plane inversion symmetry is broken. Then, using spin-to-orbital angular momentum conversion, the theory of half-integer topological charges mediated by BICs is demonstrated and experimentally proved. The same device is able to give rise to vortices with different orbital angular momentum depending on the way it is illuminated, thus improving the potential of optical multiplexing. In addition, the additive character of the topology-induced phase-vortex generation is finally demonstrated for both integer and half-integer charges using also vortex states as input beams, which is of relevance for information delivery.

1. Introduction

Polarization singularities in line fields are topological defects associated with multipolar radiation sources whose existence is protected by Poincaré–Hopf theorem.[1] The sum of the quantized topological indices, termed Hopf indices or topological charges (TCs), is an invariant.[2–7] The TC can be decomposed by fragmentation in the momentum space in more elementary singularities of half-integer indices $\pm 1/2$ associated to circularly polarized singularities known as C-points, that is, pure circular polarization states with undetermined major axis. As instance, a V-point, that is, a state with undetermined linear polarization, is the intersection of two C-lines running in opposite directions with opposite circular polarization.[8] The C-lines separate when the symmetry of the system is broken as a function of a continuously varied parameter. Thus, a V-point with TC = +1 will break into two C-points with TC = +1/2 and opposite circular polarization.

A V-point in the momentum space can also represent a dark state that cannot couple with free space radiation, and as such a bound state in the continuum (BIC).[9] In particular, V-point BICs in metasurfaces and photonic crystal slabs have been identified at the core of polarization vortices with several values of integer topological charge (TC = ±1, ±2, ...).[10–15]

BICs are localized states lying in the light cone with infinite radiative *Q*-factor as protected from free-space leakage by the associated polarization singularity.[16–22] Given the high-*Q* of these resonances, they have been applied in lasing,[21,22] non-linear frequency conversion,[23,24] ultrasensitive sensing,[25–28] fluorescence and Raman scattering enhanced spectroscopies,[29] refractometric imaging[30] and other phenomena.[31–34]

Recently, Wang *et al.* demonstrated that V-point BICs in holey lattice of silicon nitride were capable of spin-to-orbital angular momentum conversion (SOC).[13] Although occurring with trivial geometries in the direct space, BICs induce a nontrivial behavior in the momentum space, acting as reciprocal metasurfaces. The paradigm of SOC in paraxial light fields was demonstrated for the first time with an inhomogeneous birefringent element termed *q*-plate.[35] The SOC process occurs because the inhomogeneous (azimuthal) birefringent optical system converts the paraxial input polarization into an angle-varying polarization state and adding an orbital angular momentum (OAM) as a result of the geometric phase transformation. The process can flip the input photon spin, which is compensated by the variation in the OAM. This provides a light beam with a helical phase front

E. De Tommasi, S. Romano, V. Mocella, F. Sgrignuoli, G. Zito
National Research Council
Institute of Applied Sciences and Intelligent Systems "E. Caianiello"
Unit of Naples, Via P. Castellino 111, Naples I-80131, Italy
E-mail: edoardo.detommasi@na.isasi.cnr.it; gianluigi.zito@cnr.it
V. Lanzio, S. Cabrini
Lawrence Berkeley National Laboratory
Molecular Foundry Division
67 Cyclotron Road, Berkeley, California, CA 94720, USA

The ORCID identification number(s) for the author(s) of this article can be found under https://doi.org/10.1002/adom.202300475

© 2023 The Authors. Advanced Optical Materials published by Wiley-VCH GmbH. This is an open access article under the terms of the Creative Commons Attribution-NonCommercial License, which permits use, distribution and reproduction in any medium, provided the original work is properly cited and is not used for commercial purposes.

DOI: 10.1002/adom.202300475

described by an azimuthal distribution exp $(-il\phi)$, carrying OAM equal to $l\hbar$ per photon.[36,37] The value of l is related to the disclination order q, through the relation $l = \pm 2q$. As a consequence, the centre spot of the outgoing wavefront of a vortex has a phase singularity with a quantized $l = \frac{1}{2\pi}\oint_{\gamma} \nabla\phi(\mathbf{r})dr$, being γ a closed loop surrounding the topological singularity.

The similarity between SOC and BIC-based conversion of input polarization is that outgoing fields that have interacted with the resonance, with incoming/outgoing momentum encircling the V-point, assume a polarization winding in a vortex structure.[38,39] The polarization singularity has Hopf index[38,39]

$$\mathrm{TC} = \frac{1}{2\pi}\oint_{\gamma_{\mathrm{BZ}}} \nabla_{\mathbf{k}_{||}}\psi(\mathbf{k}_{||})\mathrm{d}\mathbf{k}_{||}, \tag{1}$$

where γ_{BZ} is a closed contour in the Brilluoin zone around the BIC, $\mathbf{k}_{||}$ are in-plane wave vectors, and $\psi(\mathbf{k}_{||})$ are the Poincaré angles defining the major axis orientation of the polarization ellipse at $\mathbf{k}_{||}$ in the eigenpolarization map of the radiated waves around the BIC. The spin-to-orbital angular momentum conversion produced by the interaction with BICs was first demonstrated in Ref.[13] In particular, optical vortices with $l = -2 \times \mathrm{TC} = \pm 2, \pm 4$ were experimentally observed by using a photonic crystal slab (PhCS) of Si_3N_4 supporting at-$\mathbf{\Gamma}$ BICs and provided with C_{4v} and C_{6v} symmetries, respectively.

It is interesting to notice that polarization topology emerging from BICs, BIC fragmentation due to broken symmetry, and their momentum-space distribution, is an open field of research that is expected to lead to novel designing tools in Nanophotonics. Great attention has been raised on charge splitting and merging in quasi-BICs to increase the Q-factor,[40] generating C-points,[41,42] inducing unidirectional BICs,[43] demonstrating intrinsic chiral BICs at normal incidence.[44] Recently, polariton Bose–Einstein condensation achieved at the BIC and inheriting its topological properties has also been demonstrated.[34] The potential is extraordinary when realizing that the near field properties of the BIC field, which ultimately determine the converted radiation, are a function of the geometric parameters of the system and associated energy-momentum dispersion, which therefore may be simply tuned ad hoc.

Herein, we theoretically and experimentally investigate the evolution of polarization singularities in a PhCS sustaining BICs formed near Dirac cone dispersion. Thus far, SOC studies concerned singlet sates sustaining BICs.[13,45] Polarization singularities at degenerate states with nontrivial topology like Dirac cone have been investigated in broken in-plane symmetry PhC slabs.[46] In this work instead, we study a system that has in-plane inversion symmetry but vertical asymmetry. In particular, we consider a Si_3N_4 slab layer on top of supporting SiO_2 and air cladding. We first numerically investigate the dynamics of the polarization map perturbing the condition of Dirac cone energy-momentum dispersion. When the Dirac cone forms, the radiative Dirac degenerate state appears as a V-point with TC = +1 plus two half-integer charges −1/2 at the boundaries of the Brilluoin zone, thus not detectable experimentally in far-field. In contrast, the opening of a pseudogap in the Dirac cone is accompanied by the emergence of a nonradiative BIC with spiral-polarization TC = +1 surrounded by two C-points −1/2 that exist simultaneously with the BIC close in momentum space and detectable in the far field. The total TC over the Brilluoin zone remains unvaried and equal to zero.

Such C-points with Hopf indices −1/2 are experimentally observed, for the first time, leveraging the SOC associated with such singularities, in excellent agreement with theory. The C-point interaction with the input field is explored using a low-numerical aperture converging beam, with focusing angle of ≈ 2 degrees. This analysis allow us to isolate the singularities and tune the response of the system as a function of small deviations of the incidence angle around the normal direction, observing SOC associated with different values of the topological charge. Furthermore, we demonstrate for the first time the SOC process due to the BIC also using phase vortex states having nontrivial OAM as input beams, therefore observing multiple l output states based on total angular momentum conservation. Our results are useful for engineering polarization conversion based on polarization topology and near-field properties of high-Q modes, suggesting also new tools for tuning the topological properties in light-matter interaction.[34]

2. Polarization Conversion with Half-Integer Polarization Singularity

Assuming that the PhCS behaves as a Pancharatnam–Berry phase optical elements that contains wave plates with space-variant orientation, the waves radiated with in-plane momentum

$$\boldsymbol{k}_{\parallel} \equiv (k_o \sin\theta\cos\phi, k_o \sin\theta \sin\phi),$$

once fixed θ (which fixes wavevector norm), assume polarization vectors around the V-point that rotate winding with the azimuthal incidence angle ϕ. Winding with increasing ϕ from zero to 2π, the radiated polarization is rotated by a Poincaré angle ψ a number of π-intervals equal to 2×TC. This is the same Jones transformation operated by a space-variant half-wave retarder with azimuthally rotating fast axis termed q-plate. However, this analogy is only in the effect of the transformation. In fact, at V-points, such conversion is intrinsic in the rotational symmetry of the equifrequency dispersion curve in the momentum space and does not require the inhomogeneous anisotropy in the direct space necessary in q-plates (or in resonance-based metasurfaces with azimuthal space-variant geometry[47–51]). Thus, the Hopf index TC of the polarization singularity plays the same role of the disclination order q in the inhomogeneous waveplate, TC = q. The transmitted polarization states, produced by the interaction of a focused beam onto a PhCS at the BIC frequency with TC=q, experience a different response due to the different $\mathbf{k}_{||}$ (Bloch mode) resonances. The transformation can be described in the helicity basis as

$$\begin{aligned}|E_{\mathrm{out}}\rangle = &\frac{1}{2}\left(t_x(\mathbf{k}_{||}) + t_y(\mathbf{k}_{||})\right)|E_{\mathrm{in}}\rangle \\ &+ \frac{1}{2}\left(t_x(\mathbf{k}_{||}) - t_y(\mathbf{k}_{||})\right)e^{-2iq\psi(\mathbf{k}_{||})}\langle R|E_{\mathrm{in}}\rangle|L\rangle \\ &+ \frac{1}{2}\left(t_x(\mathbf{k}_{||}) - t_y(\mathbf{k}_{||})\right)e^{+2iq\psi(\mathbf{k}_{||})}\langle L|E_{\mathrm{in}}\rangle|R\rangle. \end{aligned} \tag{2}$$

where t_x and t_y denote the (complex) transmission coefficients of each $\mathbf{k}_{||}$-Bloch mode with polarization parallel (x) and

© 2023 The Authors. Advanced Optical Materials published by Wiley-VCH GmbH

21951071, 0, Downloaded from https://onlinelibrary.wiley.com/doi/10.1002/adom.202300475 by CNR Bologna, Wiley Online Library on [06/06/2023]. See the Terms and Conditions (https://onlinelibrary.wiley.com/terms-and-conditions) on Wiley Online Library for rules of use; OA articles are governed by the applicable Creative Commons License

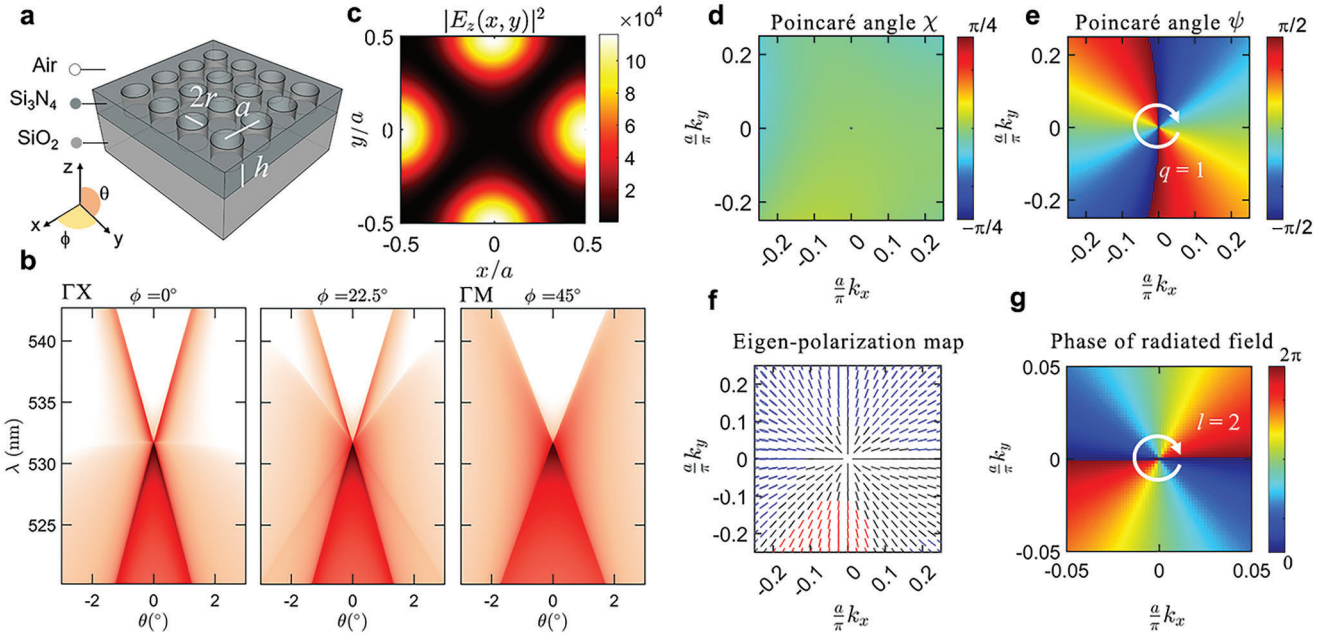

Figure 1. a) Geometry of the PhC slab. b) TM-like dispersion bands along **ΓX**, that is, ϕ = 0°, ϕ = 22.5° and **ΓM**, that is, ϕ = 45°. c) Spatial distribution of the BIC mode at 532 nm in the elementary unit cell. d) Spatial distribution of the ellipticity angle χ of the radiation field. e) Same for major axis angle ψ. f) Eigen-polarization map of the radiation field showing a V-point with $q = +1$ at the center of Brilluoin zone. g) Calculated outgoing RCP field component showing the expected phase vortex.

perpendicular (y) to an *effective* fast axis, which is one of the symmetry axes. $|E_{in}\rangle$, $|E_{out}\rangle$ are the Jones vectors of incident and transmitted light defining the full field and polarization state. Finally, $|L\rangle$, $|R\rangle$ are the left- and right-handed circularly polarized (LCP and RCP) unit vectors in the helicity basis. Equation (3) shows that the output $|E_{out}\rangle$ is a linear combination of RCP and LCP states with opposite geometric phase (Pancharatnam–Berry phase[52–54]). The latter depends on $\mathbf{k}_{||}$ and as such, with a convergent beam on the PhCS exploring all the equifrequency contour in a loop over $\mathbf{k}_{||}$, a phase vortex is obtained. It is possible to recast Equation (3) in a more compact form, defining

$$\alpha = \frac{1}{2}\left(t_x(\mathbf{k}_{||}) + t_y(\mathbf{k}_{||})\right)$$

and

$$\beta = \frac{1}{2}\left(t_x(\mathbf{k}_{||}) - t_y(\mathbf{k}_{||})\right),$$

so that

$$|E_{out}\rangle = \hat{M}\,|E_{in}\rangle\,, \tag{3}$$

with

$$\hat{M} = \alpha\,|R\rangle\,\langle R| + \alpha\,|L\rangle\,\langle L| + \beta e^{+2iq\psi}\,|R\rangle\,\langle L| + \beta e^{-2iq\psi}\,|L\rangle\,\langle R|\,. \tag{4}$$

Spin-to-orbital angular momentum conversion becomes clear if the input beam is a pure circularly polarized beam. Let be the input an LCP (RCP) state, the output will be converted in the opposite RCP (LCP) state and provided with a phase vortex of OAM in modulus equal to $|2q|$. If $|E_{in}\rangle = |L\rangle$, Equations (6-7) give

$$|E_{out}\rangle = \hat{M}|L\rangle = \alpha|R\rangle\langle R|L\rangle + \alpha|L\rangle\langle L|L\rangle + \beta e^{+2iq\psi}|R\rangle\langle L|L\rangle + \beta e^{-2iq\psi}|L\rangle\langle R|L\rangle = \alpha|L\rangle + \beta e^{+2iq\psi}|R\rangle. \tag{5}$$

The first term in Equation (7) represents the unconverted part of the input beam. The second term can be isolated projecting onto $\langle R|$ with the analyzer, which reveals experimentally the phase vortex associated with the spin-to-orbital angular momentum conversion:

$$\langle R|E_{out}\rangle = \langle R|\hat{M}|L\rangle = \alpha\langle R|L\rangle + \beta e^{+2iq\psi}\langle R|R\rangle = \beta e^{+2iq\psi}. \tag{6}$$

Similarly, if $|E_{in}\rangle = |R\rangle$, Equation (6) gives

$$|E_{out}\rangle = \hat{M}|R\rangle = \alpha|R\rangle\langle R|R\rangle + \alpha|L\rangle\langle L|R\rangle + \beta e^{+2iq\psi}|R\rangle\langle L|R\rangle + \beta e^{-2iq\psi}|L\rangle\langle R|R\rangle = \alpha|R\rangle + \beta e^{-2iq\psi}|L\rangle. \tag{7}$$

and projecting onto $\langle L|$ with the analyzer:

$$\langle L|E_{out}\rangle = \langle L|\hat{M}|R\rangle = \alpha\langle L|R\rangle + \beta e^{-2iq\psi}\langle L|L\rangle = \beta e^{-2iq\psi}. \tag{8}$$

As clear from the equations, the input spin along the propagation direction $\sigma = +\hbar$ of $|L\rangle$ would be in part converted into $\sigma = -\hbar$ of $|R\rangle$. Imposing the conservation of total angular momentum, $j\hbar = l\hbar + \sigma =$ constant, this means that the output state must have $l = +2$, which implies $l \equiv +2 \times q$ (Equation 8), as resulting from

© 2023 The Authors. Advanced Optical Materials published by Wiley-VCH GmbH

21951071, 0, Downloaded from https://onlinelibrary.wiley.com/doi/10.1002/adom.202300475 by CNR Bologna, Wiley Online Library on [06/06/2023]. See the Terms and Conditions (https://onlinelibrary.wiley.com/terms-and-conditions) on Wiley Online Library for rules of use; OA articles are governed by the applicable Creative Commons License

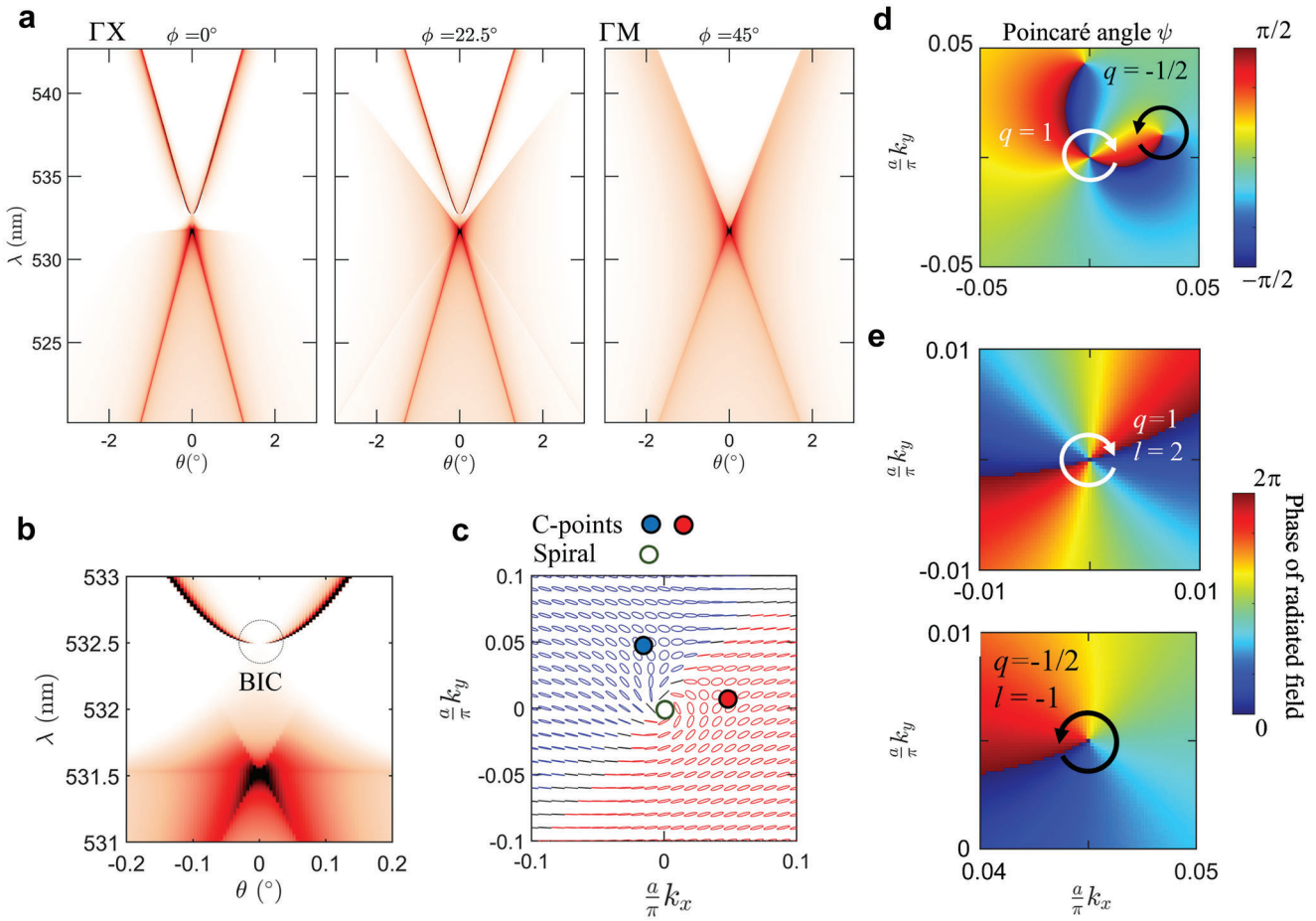

Figure 2. a) TM-like dispersion bands for h=0.17a. b) Magnified version of ***a*** along **ΓX**, showing the symmetry-protected BIC at 532.5 nm. c) Associated eigenpolarization map showing a spiral singularity with q=+1 surrounded by star-like C-points with q=−1/2. d) Map of Poincaré angle ψ of the mode in **Γ**. e) Phase vortex of the outgoing RCP field component for LCP excitation at θ=0° (top) and phase vortex of the outgoing RCP field component for LCP excitation at $k_x = 0.04(\pi/a)$, θ=1.67° (bottom).

the convention on the signs of the geometric phases chosen in Equation (3).

Now, turning to the overall efficiency of the conversion process, it must be said that given the high-Q factor of BICs, $\alpha \gg \beta$, thus the efficiency β/α is well below 100%, likely of the order of a few percent. Increment up to 86% has been recently reported.[45] Regardless of the efficiency, SOC can be used to measure the charge q of complex polarization singularity patterns, thus reveling their momentum-space topology associated to the resonance dispersion, which is the main experimental aim of this paper, for nontrivial half-integer charges.

2.1. Dirac Cone

We investigated Si_3N_4 PhCSs with square lattice on SiO_2 substrate with top cladding material index equal to 1 (air) (**Figure** 1a). Complex refractive index dispersion spectra of Si_3N_4 and SiO_2 were measured at the working slab thickness h, and used for simulations.

When the slab thickness is $h = 0.155a$ (a lattice period), two singlet states merge at the degenerate **Γ** point with linear dispersion, forming a Dirac cone, as shown in Figure 1b. The p-polarization dispersion diagram (i.e., TM-like modes) and associated mode profiles, at a given λ and in-plane momentum $\boldsymbol{k}_{\parallel}$, were obtained from transmittance simulations carried out with rigorous coupled waves approach (Ansys Lumerical 2022, RCWA module). The BIC vector field reported in Figure 1c, was retrieved perturbing normal incidence excitation, that is, was computed for an incident angle $\theta = \pm 0.01°$, which corresponds to $k_x = \pm 2.4 \times 10^{-4}\pi/a$. It is worth mentioning that no in-plane broken inversion symmetry has been introduced in the geometry, in contrast to Ref. [46]

As the bands touch at normal incidence, the doubly degenerate mode acquires a nontrivial TC, which keeps the local field intensity $|E_z|^2/|E_0|^2$ ($E_0 = 1$) highly enhanced as shown in Figure 1c. We ascribe this behavior to the fact that the superior band shows a BIC when the cone opens, and in that case the maximum ~10^4 here shown is actually limited only by the finite spectral resolution of the simulation, as the maximum resulted >10^8 upon iterative search of the highest field frequency. The polarization topology is more easily readable in the maps of Poincaré angles (χ, ψ) shown in Figure 1d–e and calculated from Stokes parameters of the far field projected onto the plane normal to each di-

© 2023 The Authors. Advanced Optical Materials published by Wiley-VCH GmbH

21951071, 0, Downloaded from https://onlinelibrary.wiley.com/doi/10.1002/adom.202300475 by CNR Bologna, Wiley Online Library on [06/06/2023]. See the Terms and Conditions (https://onlinelibrary.wiley.com/terms-and-conditions) on Wiley Online Library for rules of use; OA articles are governed by the applicable Creative Commons License

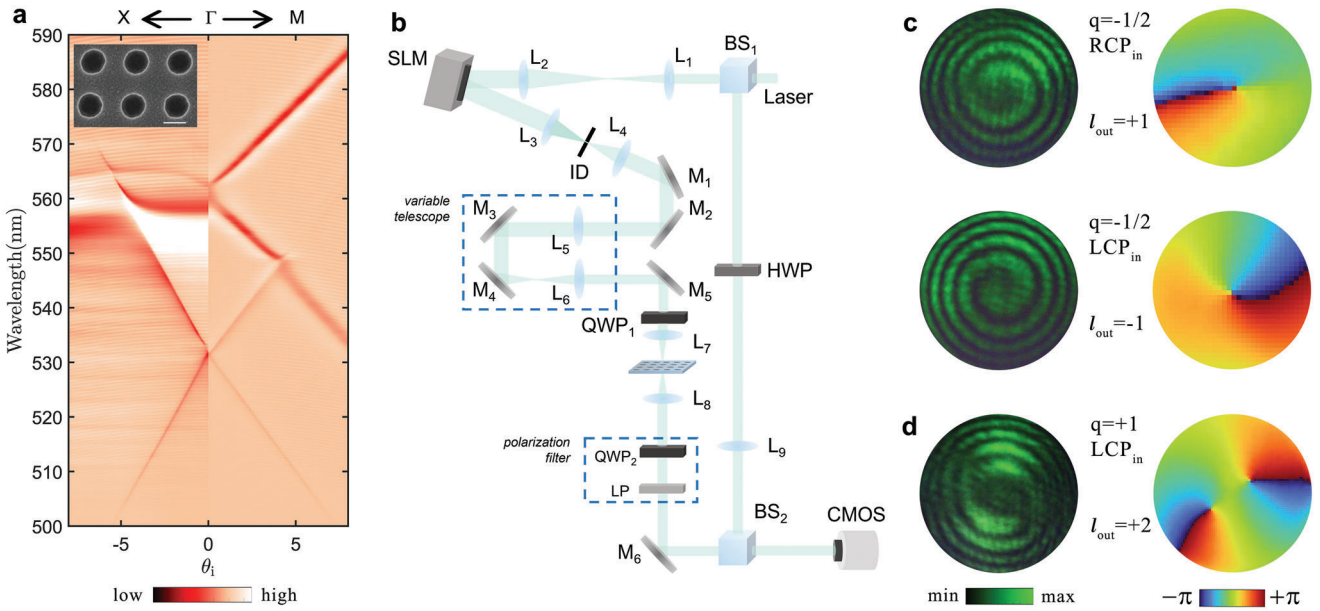

Figure 3. a) Experimental band diagram of the sample. Inset: scanning electron microscopy image of the sample (scalebar = 200 nm). b). Scheme of the interferometric setup and SLM system. $BS_{1,2}$: beam-splitters; M: mirror; L_{1-9}: lenses; SLM: spatial light modulator; ID: iris diaphgram; $QWP_{1,2}$: quarter-wave plates; LP: linear polarizer; HWP: half-wave plate. c,d) Interference with spherical-wave reference (left) and retrieved phase distributions (right) of the converted circularly-polarized component emerging from the PhCS out **Γ**-point (c) and at normal incidence (d).

rection $\boldsymbol{k}_z + \boldsymbol{k}_{||}$. The ellipticity angle χ, which must have values in the range $(-\pi/4, \pi/4)$, is maximum just in correspondence with $s_3 = \pm 1$ (RCP and LCP states, respectively), whereas for linear polarization $\chi = 0$ (Figure 1d). On the other hand, the map of ellipse major axis ψ, admitting values in the range $(-\pi/2, \pi/2)$, individuates clearly the TCs. Two clockwise π loops in ψ are equivalent to a 2π loop of the polarization, giving $q = +1$ (Figure 1e). The excited mode shows a singularity in the polarization pattern arising at the Dirac point along normal incidence. The eigenpolarization map was calculated using a custom-built MathWorks Matlab code following the explicit method used to obtain the far-field polarization states in Ref. [55]. The map reported in Figure 1f shows a linear polarization V-point near **Γ**.[56] Indeed, the associated Poincaré angles χ is equal to zero, as shown in Figure 1d, and it is characterized by a topological charge q equal to +1, as ψ winds clockwise for two times in Figure 1e. However, it must be said that two half integer charges −1/2 appear at the boundaries of the Brilluoin zone $(\pm\pi/a)$, thus over the whole zone the total TC = 0.

Figure 1g also shows the calculated optical field radiated by such singular mode. The phase vortex is calculated using LCP polarization as the input plane wave to excite the resonance at the BIC frequency, then the radiated field is projected onto the RCP component and its phase retrieved, following Equations (6) and (7). Since $q = +1$, the outgoing field have a vortex phase with OAM $l = 2$, as shown in Figure 1g.

2.2. Removing Dirac Degeneracy and Emergence of Half-Integer Singularities

The main result of our numerical investigation appears when $h = 1.70a$, the ideal Dirac cone condition is perturbed and the linear dispersion is broken. The lower energy band acquires a zero tangent at normal incidence, distant 0.5 nm from the other band, as shown in **Figure 2**a,b. Therefore, while the bands are degenerate only at the specific incidence angle along **ΓM** direction, a pseudogap opens along **ΓX** as highlighted in the magnified dispersion shown in Figure 2b. The lower energy mode (longer wavelength) becomes a quadrupolar symmetry-protected BIC, as aforementioned, that we term, in brief, quasi-Dirac BIC to stress its origin. In addition to the quasi-Dirac BIC forming at **Γ**, two peripheral disclinations appear in eingenpolarization map shown in Figure 2c. The map of the Poincaré angle ψ, reported in Figure 2d, identifies two clear C-points. Moreover, Figure 2d shows a π-counterclockwise rotation of the ψ angle, that is, a π-loop of polarization associated with TC = -1/2. Since the corresponding $\chi = \pm\pi/4$ (not shown), we can conclude that the identified points are circular polarization singularities. These C-points have opposite helicities and same star-type topology (-1/2). As visible in Figure 2c, they surround the spiral singularity with charge +1.

The position of the C-points was found symmetric with respect to the excitation angle. The case of positive incidence $\theta = 0.01°$ is shown in Figure 2c,d. These results would be mirrored in the momentum-space at the symmetric position with respect to zero as the incidence angle used to calculate the mode is negative, $\theta = -0.01°$.

In synthesis, when perturbing the system, the Dirac cone opens, the at-**Γ** BIC stems from the degeneracy removal, a spiral vortex with $q = 1$ and two circularly polarized singularities with half-integer topological charge −1/2 are radiated by the quasi-Dirac BIC. These half-integer singularities produce a new effect, enabling spin-to-orbital angular momentum conversion with $|q| = 1/2$, which would provide phase vortices with $|l| = 1$. Indeed,

© 2023 The Authors. Advanced Optical Materials published by Wiley-VCH GmbH

21951071, 0, Downloaded from https://onlinelibrary.wiley.com/doi/10.1002/adom.202300475 by CNR Bologna, Wiley Online Library on [06/06/2023]. See the Terms and Conditions (https://onlinelibrary.wiley.com/terms-and-conditions) on Wiley Online Library for rules of use; OA articles are governed by the applicable Creative Commons License

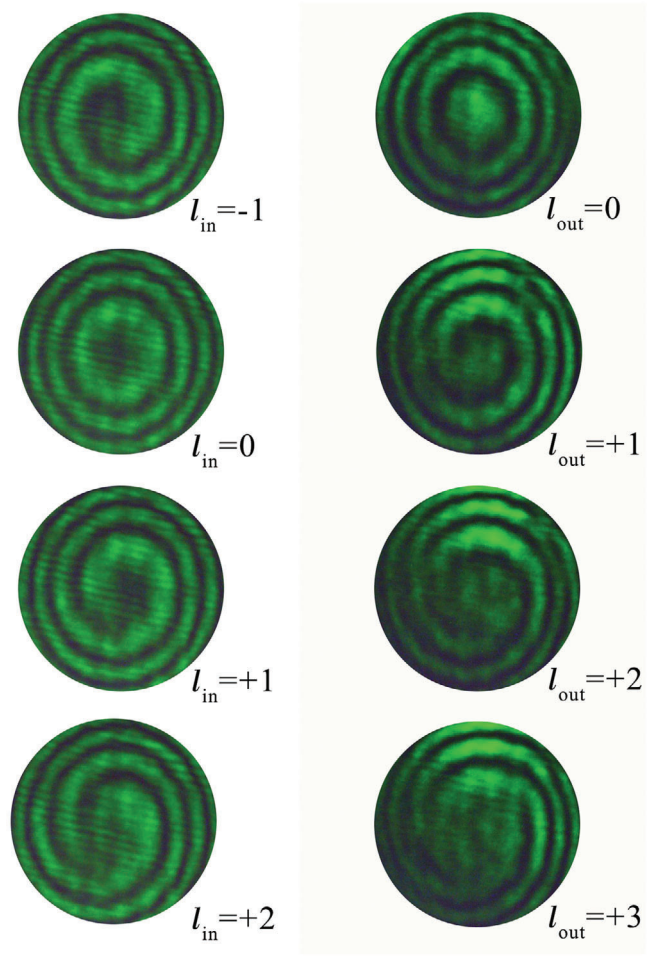

Figure 4. First column: interference patterns of the optical vortices generated by the SLM with increasing topological charge l_{in}. Second column: corresponding interference patterns of the helical mode emerging from the PhCS after interaction with the optical vortices generated by the SLM. The topological charge of the helical mode is given by $l_{out} = l_{in} + 1$.

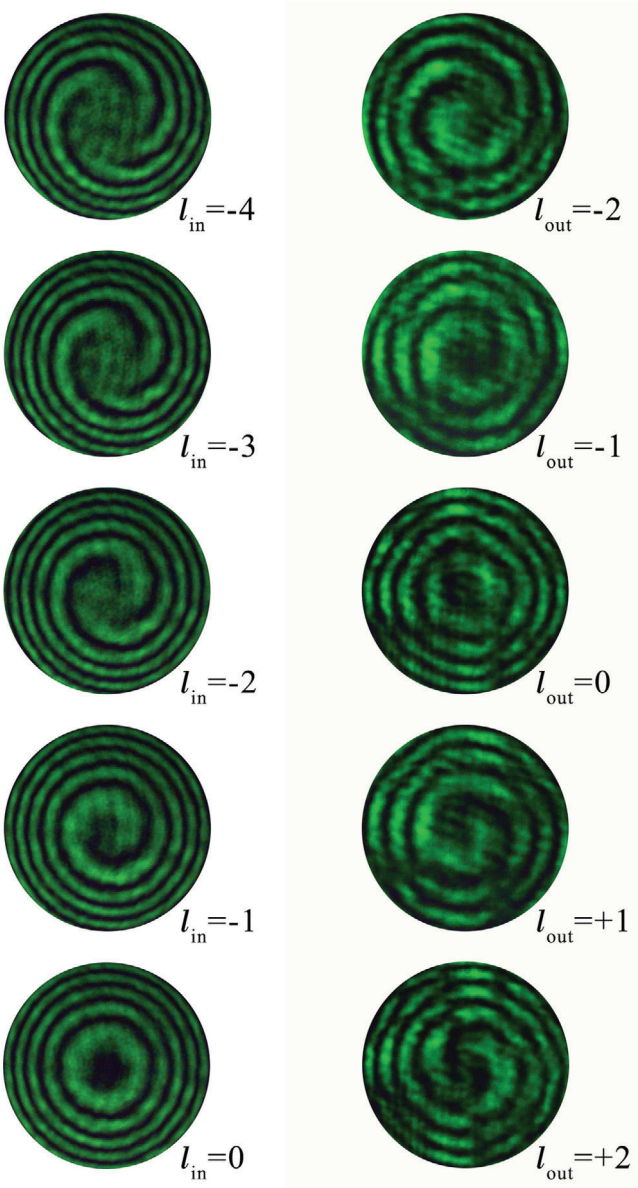

Figure 5. First column: interference patterns of the optical vortices generated by the SLM with increasing topological charge l_{in}. Second column: corresponding interference patterns of the helical mode emerging from the PhCS after interaction with the expanded optical vortices generated by the SLM. The topological charge of the helical mode now is given by $l_{out} = l_{in} + 2$.

as shown in Figure 2e (top), when the central charge $q = +1$ is considered, the input LCP field is converted into RCP generating a phase vortex with $l = 2$ as expected. In contrast, when the half-integer singularity is excited with input wavevector surrounding the singular point, the input LCP field is converted into RCP with a phase vortex equal to $l = -1$, as shown in Figure 2e (bottom), and $l = +1$ for RCP input. This is the new effect that we investigated also experimentally, as discussed below.

2.3. Experimental Demonstration of Half-Integer Polarization Singularities

We experimentally studied the pseudogap condition reached when $a = 360$ nm and $h = 0.17a$ leveraging the spin-to-orbital angular momentum conversion expected as a result of interaction with the polarization singularity. We recall that a polarization singularity in the momentum space, TC = q, will induce a doubled vortex phase singularity, $l = +2q$, in the RCP outgoing radiation and $l = -2q$ in the LCP outgoing radiation after interaction with the PhCS. In addition, we also considered the possibility of exciting the PhCS topological singularity with a vortex phase beam in input, that is, already endowed with nontrivial l, in order to demonstrate the general additive property of quantized OAM for both reciprocal-space polarization singularities $q = +1$ and $q = -1/2$.

The holey square lattice in Si_3N_4 was patterned over an area of 1 mm^2 by means of electron beam lithography combined with a plasma etching process according to previous methods.[30] Angle-resolved transmittance spectra as a function of the incidence

© 2023 The Authors. Advanced Optical Materials published by Wiley-VCH GmbH

21951071, 0, Downloaded from https://onlinelibrary.wiley.com/doi/10.1002/adom.202300475 by CNR Bologna, Wiley Online Library on [06/06/2023]. See the Terms and Conditions (https://onlinelibrary.wiley.com/terms-and-conditions) on Wiley Online Library for rules of use; OA articles are governed by the applicable Creative Commons License

21951071, 0, Downloaded from https://onlinelibrary.wiley.com/doi/10.1002/adom.202300475 by CNR Bologna, Wiley Online Library on [06/06/2023]. See the Terms and Conditions (https://onlinelibrary.wiley.com/terms-and-conditions) on Wiley Online Library for rules of use; OA articles are governed by the applicable Creative Commons License

angle θ were acquired and the dispersion diagrams retrieved.[27,29] **Figure 3**a shows the experimental band diagram for *p*-polarized incidence (i.e., TM-like modes), which is in excellent agreement with the simulations reported in Figure 2a,b. Moreover, Figure 3a displays the formation of the BIC at 532 nm along $\mathbf{\Gamma X}$ direction, whereas the bands touch at 532 nm along $\mathbf{\Gamma M}$. The inset shows a representative SEM image of the PhCS. The value of h was measured by means of variable-angle spectroscopic ellipsometry and atomic force microscopy and resulted 62 nm, in agreement with the requirement $h = 0.17a$.

To measure the vortex charge l, we made use of the interferometric setup schematized in Figure 3b (see also Experimental Section for more details). A spatial light modulator (SLM) was placed in the path of the signal beam, which allowed generating homogeneously polarized optical vortices with arbitrary topological charge l. The laser beam was suitably expanded and collimated by a variable telescope, then focused on the sample with convergence angle of about 2°. This control allowed us to vary the explored region of momentum space. The telescope was bypassed on demand with a flip mirror. The PhCS sample was first shined by RCP laser beam resonant with the BIC mode at $\lambda = 532$ nm, while the outcoming radiation was collected and superimposed to the reference beam after being properly filtered to allow the transmission of the sole LCP component produced by SOC. The interferograms were acquired varying the angle of incidence in order to match $q = +1$ at $\theta = 0$ and $q = -1/2$ expected at $\theta \simeq 1.67°$. Figure 3c shows the SOC effect associated with $q = -1/2$ for RCP and LCP input, respectively. In the second column, the corresponding phase distributions determined by using the approach reported in Ref. [57] are shown. For RCP input, the interferometric pattern of converted-LCP state consists of a spiral lobe wrapped clockwise ($l = -2 \times (-1/2) = +1$), while for LCP input the vortex flips the winding direction ($l = -1$) (see Equations 6–9). Analogous results were obtained when tilting the sample along vertical axis $\hat{\mathbf{y}}$, due to the symmetry of the PhCS.

Figure 3d shows that when the probing beam matches normal incidence, a second arm starts emerging in a clockwise wrapped spiral pattern, $l = 2 \times (+1) = +2$ for LCP incident radiation, in accordance with previous observations for a C_{4v} PhCS supporting a nondegenerate singlet BIC.[13] The second column of Figure 3c shows the phase maps reconstructed from the interferograms following the method reported in Ref. [57] (see also Experimental Section for details).

2.4. Additive Character of OAM Generated by Reciprocal-Space Polarization Singularity

When the input beam has OAM l_{in}, say $|E_{\text{in}}\rangle = |E_o\rangle\, e^{il_{in}\Psi}$, we can include the orbital phase factor into the optical Jones transformation. If $|E_{\text{in}}\rangle = |R\rangle\, e^{il_{in}\Psi}$, since the intrinsic conversion in the outgoing $|L\rangle$ component creates $l = l_{BIC} = 2q$ (Equation 1), the overall effect of polarization transform $\hat{M}$ and filtering onto $\langle L|$ of the converted component will provide

$$\begin{aligned}\langle L|M|R\rangle e^{il_{in}\Psi} &= \alpha\langle L|R\rangle e^{il_{in}\Psi} + \beta e^{+2iq\Psi} e^{il_{in}\Psi}\langle L|L\rangle \\ &= \beta e^{i(2q+l_{in})\Psi} = \beta e^{il_{out}\Psi} \end{aligned} \quad (9)$$

in which we used $l_{out} = 2q + l_{in} = l_{BIC} + l_{in}$. To the best of our knowledge, while this effect is known for direct-space Pancharatnam optical elements, it has never been experimentally verified before in case of momentum-space conversion enabled by metasurfaces sustaining BICs. In the following, we show the results achieved in our experiments. In order to investigate this effect, the PhCS was interrogated with OAM beams generated by the SLM as a function of l_{in}. **Figure 4** shows the additive character of the quantized OAM when exciting with RCP input the polarization singularity $q = -1/2$ after filtering the outgoing converted LCP component $l_{BIC} = -2 \times (-1/2) = +1$. As clearly visible, the effect is well verified for all values of l_{in}. Similarly, **Figure 5** shows the OAM additive character when exciting the polarization singularity $q = +1$ with LCP input, after filtering the outgoing converted RCP component $l_{BIC} = +2q = +2$. Again, the additive effect is well verified for all values of l_{in}. Of course, flipping the input helicity was systematically associated with the inversion of the outgoing phase vortex.

3. Conclusion

In conclusion, we theoretically and experimentally investigated the evolution of polarization singularities in a PhCS sustaining a BIC formed near Dirac cone dispersion by using the spin-to-orbital angular momentum conversion produced in the momentum space. We showed the evolution of the polarization map of the near normal-incidence mode as the Dirac cone is approached with varying slab thickness h, revealing the existence of half-integer topological charges in the polarization field radiated by the quasi-Dirac BIC in addition to the known integer charge. It worth mentioning indeed that the half-integer charges are not produced by the BIC charge fragmentation. Charge fragmentation corresponds to the well-known case when the BIC integer charge +1 splits into two half-integer +1/2, of equal sign, upon in-plane inversion symmetry breaking (as for instance in a lattice of triangular holes[58]). In our case, the system of integer and opposite-sign half-integer charges are peculiar of the dispersion properties of the pseudogap formed when the Dirac degeneracy is removed and associated with this specific quasi-Dirac BIC.

Then, such C-points with Hopf index −1/2 were experimentally observed in the polarization conversion induced by the quasi-Dirac BIC in the momentum space. This was achieved leveraging the SOC associated with such polarization singularity. We demonstrated that the same device is able to give rise to vortices with different OAM values depending on the way it is illuminated, improving its potential in optical multiplexing by expanding information capability. Furthermore, we experimentally demonstrated the additive character of the singularity-induced SOC with nontrivial OAM input states, of relevance for information delivery. Since the BICs are high-Q resonances applied in lasing,[21,22] non-linear frequency conversion[23,24] and other phenomena,[31–34] engineering the polarization conversion based on singular BICs can find application for tuning the topological properties in light-matter interaction, enabling controlled light polarization conversion for far field light sources or integrated photonic circuits. Here, we have shown some potential of this effect.

© 2023 The Authors. Advanced Optical Materials published by Wiley-VCH GmbH

4. Experimental Section

In order to detect SOC induced by the designed PhCS, the interferometric setup described in Figure 3b was used. A *p*-polarized beam from a diode laser (DPSS LaserSTL emitting at $\lambda = 532$ nm, $P_{out} = 150$ mW) was split into a signal and a reference beam by a 50/50 beam splitter (BS_1). A spatial light modulator (LCOS-SLM Hamamatsu X13138 series, resolution: 1272×1024 pixel, active area: 16×12.8 mm^2) was placed in the path of the signal beam, which allows generating optical vortices with an arbitrary topological charge *l* to be injected into the PhCS. In detail, the laser beam was first spatially filtered and expanded by a 20× telescope (formed by lenses L_1 and L_2 in figure) in order to completely fill the active area of the SLM. The SLM was addressed by a 8-bit grayscale, computer-generated mask corresponding to the pitch-forked phase profile of a Laguerre–Gauss mode of given topological charge *l*. Two lenses (L_3 and L_4) were placed along the optical path in a 4*f* configuration.[59] An iris diaphgram (ID in figure) was placed between lenses L_3 and L_4 in order to select only the first-order diffraction of the beam modulated by the SLM. A variable telescope, formed by the lens L_5 and L_6 allows to change the dimension of the beam. The signal beam passes through a quarter-wave plate (QWP_1) oriented in order to produce a circularly-polarized beam with the desired helicity which was then focused on the PhCS by a lens (L_7). The device was mounted on a roto-translational stage in order to control both the region to be probed and the angle of incidence. The outcoming light was collected by a second lens (L_8) positioned in nearly telescopic configuration in order to give rise to a slightly divergent beam provided with a spherical wavefront. A second quarter-wave plate (QWP_2) with orthogonal fast axis with respect to QWP_1, in combination with a linear polarizer (LP) oriented at 90° with respect to laser polarization, allows transmitting only the polarization handedness opposite to the initial one, thus filtering out the background field that does not undergo spin-to-orbit conversion. A half-wave plate (HWP) was used to rotate the polarization state of the reference beam from *p* to *s*, in order to increase the fringe contrast of the interference pattern. Finally, signal and reference beam (which passes through a lens (L_9) to obtain a spherical wavefront) were recombined by the beam splitter BS_2 and sent to a CMOS camera (IDS model UI-1240SE-C-HQ, 1280×1024 pixel array) for the detection of the interference pattern. Focal lengths: $f_1 = 2.5$ cm; $f_2 = 50$; $f_3 = f_4 = 30$; $f_5 = 50$, and $f_6 = 10$ cm (when the telescope was inserted in the optical path); $f_7 = f_8 = 15$; $f_9 = 10$ cm.

Acknowledgements

The authors are thankful to Scott Dhuey, Molecular Foundry, Lawrence Berkeley National Laboratory, USA, for assistance in the fabrication process. Financial support from the project PIT-STOP grant no. PRIN-2017-20173CRP3H, MUR, Italy is acknowledged. The work at the Molecular Foundry was supported by the Office of Science, Office of Basic Energy Sciences, of the U.S. Department of Energy under Contract No. DE-AC02-05CH11231.

Conflict of Interest

The authors declare no conflict of interest.

Data Availability Statement

The data that support the findings of this study are available from the corresponding author upon reasonable request.

Keywords

bound states in the continuum, Dirac cone, half-integer topological charge, optical vortex, spin-to-orbital angular momentum conversion

Received: February 24, 2023
Revised: April 27, 2023
Published online:

[1] W. Liu, W. Liu, L. Shi, Y. Kivshar, *Nanophot.* **2021**, *10*, 1469.
[2] I. Freund, *Opt. Comm.* **2002**, *201*, 251.
[3] W. Chen, Y. Chen, W. Liu, *Las. Phot. Rev.* **2020**, *14*, 2000049.
[4] P. Senthilkumaran, S. K. Pal, P. S. Ruchi, *Int. J. Opt.* **2020**, *2020*, 2812803.
[5] F. Wang, X. Yin, Z. Zhang, Z. Chen, H. Wang, P. Li, Y. Hu, X. Zhou, C. Peng, *Front. Phys.* **2022**, 198.
[6] V. V. Kotlyar, A. A. Kovalev, V. D. Zaitsev, *Photonics* **2022**, *9*, 298.
[7] H. Price, Y. Chong, A. Khanikaev, H. Schomerus, L. J. Maczewsky, M. Kremer, M. Heinrich, A. Szameit, O. Zilberberg, Y. Yang, B. Zhang, A. Alú, R. Thomale, I. Carusotto, P. St-Jean, A. Amo, A. Dutt, L. Yuan, S. Fan, X. Yin, C. Peng, T. Ozawa, A. Blanco-Redondo, *J. Phys.: Photonics* **2022**, *4*, 032501.
[8] J. Peng, R.-Y. Zhang, S. Jia, W. Liu, S. Wang, *Sci. Adv.* **2022**, *8*, eabq0910.
[9] C. W. Hsu, B. Zhen, J. Lee, S.-L. Chua, S. G. Johnson, J. D. Joannopoulos, M. Soljačić, *Nature* **2013**, *499*, 188.
[10] B. Zhen, C. W. Hsu, L. Lu, A. D. Stone, M. Soljačić, *Phys. Rev. Lett.* **2014**, *113*, 257401.
[11] H. M. Doeleman, F. Monticone, W. den Hollander, A. Alù, A. F. Koenderink, *Nat. Phot.* **2018**, *12*, 397.
[12] T. Yoda, M. Notomi, *Phys. Rev. Lett.* **2020**, *125*, 053902.
[13] B. Wang, W. Liu, M. Zhao, J. Wang, Y. Zhang, A. Chen, F. Guan, X. Liu, L. Shi, J. Zi, *Nat. Photonics* **2020**, *14*, 623.
[14] S. I. Azzam, A. V. Kildishev, *Adv. Opt. Mater.* **2021**, *9*, 2001469.
[15] K. Bliokh, E. Karimi, M. Padgett, M. Alonso, M. Dennis, A. Dudley, A. Forbes, S. Zahedpour, S. Hancock, H. Milchberg, S. Rotter, F. Nori, Ş. K. Özdemir, N. Bender, H. Cao, P. B. Corkum, C. Hernández-García, H. Ren, Y. Kivshar, M. G. Silveirinha, N. Engheta, A. Rauschenbeutel, P. Schneeweiss, J. Volz, D. Leykam, D. A. Smirnova, K. Rong, B. Wang, E. Hasman, M. F. Picardi, et al., *arXiv preprint arXiv:2301.* **2023**, 05349.
[16] H. Friedrich, D. Wintgen, *Phys. Rev. A* **1985**, *32*, 3231.
[17] J. Von Neumann, E. Wigner, *Phys. Z* **1929**, *30*, 465.
[18] S. Joseph, S. Pandey, S. Sarkar, J. Joseph, *Nanophotonics* **2021**, *10*, 4175.
[19] V. Mocella, S. Romano, *Phys. Rev. B* **2015**, *92*, 155117.
[20] E. De Tommasi, E. Esposito, S. Romano, A. Crescitelli, V. Di Meo, V. Mocella, G. Zito, I. Rendina, *La Rivista del Nuovo Cimento* **2021**, *44*, 1.
[21] A. Kodigala, T. Lepetit, Q. Gu, B. Bahari, Y. Fainman, B. Kanté, *Nature* **2017**, *541*, 196.
[22] C. Huang, C. Zhang, S. Xiao, Y. Wang, Y. Fan, Y. Liu, N. Zhang, G. Qu, H. Ji, J. Han, L. Ge, Y. Kivshar, Q. Song, *Science* **2020**, *367*, 1018.
[23] N. Bernhardt, K. Koshelev, S. J. White, K. W. C. Meng, J. E. Froch, S. Kim, T. T. Tran, D.-Y. Choi, Y. Kivshar, A. S. Solntsev, *Nano Lett.* **2020**, *20*, 5309.
[24] K. Koshelev, S. Kruk, E. Melik-Gaykazyan, J.-H. Choi, A. Bogdanov, H.-G. Park, Y. Kivshar, *Science* **2020**, *367*, 288.
[25] S. Romano, G. Zito, S. Torino, G. Calafiore, E. Penzo, G. Coppola, S. Cabrini, I. Rendina, V. Mocella, *Photonics Res.* **2018**, *6*, 726.
[26] F. Yesilkoy, E. R. Arvelo, Y. Jahani, M. Liu, A. Tittl, V. Cevher, Y. Kivshar, H. Altug, *Nat. Photonics* **2019**, *13*, 390.
[27] G. Zito, G. Sanità, B. G. Alulema, S. N. L. Yépez, V. Lanzio, F. Riminucci, S. Cabrini, M. Moccia, C. Avitabile, A. Lamberti, , V. Mocella, I. Rendina, S. Romano, *Nanophotonics* **2021**, *10*, 4279.
[28] C. Schiattarella, G. Sanità, B. G. Alulema, V. Lanzio, S. Cabrini, A. Lamberti, I. Rendina, V. Mocella, G. Zito, S. Romano, *Biosens. Bioelectron.: X* **2022**, *12*, 100262.

© 2023 The Authors. Advanced Optical Materials published by Wiley-VCH GmbH

21951071, 0, Downloaded from https://onlinelibrary.wiley.com/doi/10.1002/adom.202300475 by CNR Bologna, Wiley Online Library on [06/06/2023]. See the Terms and Conditions (https://onlinelibrary.wiley.com/terms-and-conditions) on Wiley Online Library for rules of use; OA articles are governed by the applicable Creative Commons License

[29] S. Romano, G. Zito, S. Managò, G. Calafiore, E. Penzo, S. Cabrini, A. C. De Luca, V. Mocella, *J. Phys. Chem* **2018**, *122*, 19738.
[30] S. Romano, M. Mangini, E. Penzo, S. Cabrini, A. C. De Luca, I. Rendina, V. Mocella, G. Zito, *ACS nano* **2020**, *14*, 15417.
[31] G. Zito, S. Romano, S. Cabrini, G. Calafiore, A. C. De Luca, E. Penzo, V. Mocella, *Optica* **2019**, *6*, 1305.
[32] T. Wang, Z. Li, X. Zhang, *Photonics Res.* **2019**, *7*, 341.
[33] T. Santiago-Cruz, S. D. Gennaro, O. Mitrofanov, S. Addamane, J. Reno, I. Brener, M. V. Chekhova, *Science* **2022**, *377*, 991.
[34] V. Ardizzone, F. Riminucci, S. Zanotti, A. Gianfrate, M. Efthymiou-Tsironi, D. Suàrez-Forero, F. Todisco, M. De Giorgi, D. Trypogeorgos, G. Gigli, K. Baldwin, L. Pfeiffer, D. Ballarini, H. S. Nguyen, D. Gerace, D. Sanvitto, *Nature* **2022**, *605*, 447.
[35] L. Marrucci, C. Manzo, D. Paparo, *Phys. Rev. Lett.* **2006**, *96*, 163905.
[36] J. F. Nye, M. V. Berry, in *A Half-Century of Physical Asymptotics and Other Diversions: Selected Works by Michael Berry*, World Scientific, Singapore **1974**, pp. 6–31.
[37] L. Allen, M. W. Beijersbergen, R. Spreeuw, J. Woerdman, *Phys. Rev. A* **1992**, *45*, 8185.
[38] Y. Zhang, A. Chen, W. Liu, C. W. Hsu, B. Wang, F. Guan, X. Liu, L. Shi, L. Lu, J. Zi, *Phys. Rev. Lett.* **2018**, *120*, 186103.
[39] H. M. Doeleman, F. Monticone, W. den Hollander, A. Alù, A. F. Koenderink, *Nat. Photonics* **2018**, *12*, 397.
[40] M. Kang, S. Zhang, M. Xiao, H. Xu, *Phys. Rev. Lett.* **2021**, *126*, 117402.
[41] T. Shi, Z.-L. Deng, G. Geng, Y. Zeng, G. Hu, A. Overvig, J. Li, C.-W. Qiu, A. Alù, Y. S. Kivshar, X. Li, *Nat. Commun.* **2022**, *13.1*, 4111.
[42] X. Zhang, Y. Liu, J. Han, Y. Kivshar, Q. Song, *Science* **2022**, *377*, 1215.
[43] X. Yin, J. Jin, M. Soljačić, C. Peng, B. Zhen, *Nature* **2020**, *580*, 467.
[44] Y. Chen, H. Deng, X. Sha, W. Chen, R. Wang, Y.-H. Chen, D. Wu, J. Chu, Y. S. Kivshar, S. Xiao, C.-W. Qiu, *Nature* **2023**, *613*, 474.
[45] T. Li, J. Wang, W. Zhang, X. Wang, W. Liu, L. Shi, J. Zi, *Nat. Sci. Rev.* **2023**, *10.5*, nwac234.
[46] A. Chen, W. Liu, Y. Zhang, B. Wang, X. Liu, L. Shi, L. Lu, J. Zi, *Phys. Rev. B* **2019**, *99*, 180101.
[47] A. V. Kildishev, A. Boltasseva, V. M. Shalaev, *Science* **2013**, *339*, 6125.
[48] N. Yu, F. Capasso, *Nat. Mater.* **2014**, *13*, 139.
[49] R. C. Devlin, A. Ambrosio, D. Wintz, S. L. Oscurato, A. Y. Zhu, M. Khorasaninejad, J. Oh, P. Maddalena, F. Capasso, *Opt. Express* **2017**, *25*, 377.
[50] R. C. Devlin, A. Ambrosio, N. A. Rubin, J. B. Mueller, F. Capasso, *Science* **2017**, *358*, 896.
[51] T. Liu, W. Li, Y. Meng, H. Ma, W. Tang, G. Li, H. Shi, S. Sui, J. Wang, S. Qu, *Adv. Opt. Mater.* **2022**, *10*, 2102638.
[52] S. Pancharatnam, in *Proceedings of the Indian Academy of Sciences-Section A*, Vol. *44*, Springer, Berlin **1956**, pp. 398–417.
[53] M. V. Berry, *Proc. R. Soc. London, A* **1984**, *392*, 45.
[54] G. Milione, H. Sztul, D. Nolan, R. Alfano, *Phys. Rev. Lett.* **2011**, *107*, 053601.
[55] W. Ye, Y. Gao, J. Liu, *Phys. Rev. Lett.* **2020**, *124*, 153904.
[56] P. Senthilkumaran, *Front. Phys.* **2020**, *8*, 140.
[57] T. Latychevskaia, H.-W. Fink, *Appl. Opt.* **2015**, *54*, 2424.
[58] J. Wang, M. Zhao, W. Liu, F. Guan, X. Liu, L. Shi, C. T. Chan, J. Zi, *Nat. Commun.* **2021**, *12*, 6046.
[59] G. Pesce, G. Volpe, O. M. Maragó, P. H. Jones, S. Gigan, A. Sasso, G. Volpe, *JOSA B* **2015**, *32*, B84.

© 2023 The Authors. Advanced Optical Materials published by Wiley-VCH GmbH

21951071, 0, Downloaded from https://onlinelibrary.wiley.com/doi/10.1002/adom.202300475 by CNR Bologna, Wiley Online Library on [06/06/2023]. See the Terms and Conditions (https://onlinelibrary.wiley.com/terms-and-conditions) on Wiley Online Library for rules of use; OA articles are governed by the applicable Creative Commons License